

Cooling the Coldest Continent

The 4 December 2021 Total Solar Eclipse over Antarctica

René Garreaud, Deniz Bozkurt, Carl Spangrude, Tomás Carrasco-Escaff, Roberto Rondanelli, Ricardo Muñoz, Xavier M. Jubier, Matthew Lazzara, Linda Keller, and Patricio Rojo®

KEYWORDS:

Antarctica; Energy budget/ balance; Regional effects; Surface observations; Numerical analysis/ modeling

ABSTRACT: Total solar eclipses (TSEs) are impressive astronomical events that have attracted people's curiosity since ancient times. Their abrupt alterations to the radiation balance have stimulated studies on "eclipse meteorology," most of them documenting events in the Northern Hemisphere while only one TSE (23 November 2003) has been described over Antarctica. On 4 December 2021—just a few days before the austral summer solstice—the moon blocked the sun over the austral high latitudes, with the path of totality arching from the Weddell Sea to the Amundsen Sea, thus producing a \sim 2-min central TSE. In this work we present high-resolution meteorological observations from Union Glacier Camp (80°S, 83°W), the only location with a working station under totality, and South Pole station. These observations were complemented with meteorological records from 37 surface stations across Antarctica. Notably, the largest cooling (\sim 5°C) was observed over the East Antarctic dome, where obscurity was \sim 85% while many sectors experienced insignificant temperature changes. This heterogenous cooling distribution, at odds with the seemingly homogeneous land surface of Antarctica, is partially captured by a simple radiative model. To further diagnose the effect of the eclipse on the surface meteorology, we ran multiple pairs of simulations (eclipse enabled and disabled) using the Weather Research and Forecasting (WRF) Model. The overall pattern and magnitude of the simulated cooling agree well with the observations and reveal that, in addition to the solar radiation deficit and cloud cover, low-level winds and the height of the planetary boundary layer are key determinants of the temperature changes and their spatial variability.

https://doi.org/10.1175/BAMS-D-22-0272.1

Corresponding author: Patricio Rojo, pato@das.uchile.cl

Supplemental material: https://doi.org/10.1175/BAMS-D-22-0272.2

In final form 18 August 2023

© 2023 American Meteorological Society. This published article is licensed under the terms of the default AMS reuse license. For information regarding reuse of this content and general copyright information, consult the AMS Copyright Policy (www.ametsoc.org/PUBSReuseLicenses).

AFFILIATIONS: Garreaud and Rondanelli—Geophysics Department, and Center for Climate and Resilience Research, Universidad de Chile, Santiago, Chile; Bozkurt—Center for Climate and Resilience Research, Universidad de Chile, Santiago, and Meteorology Department, Universidad de Valparaíso, Valparaíso, Chile; Spangrude—Montana Space Grant, Missoula, Montana; Carrasco-Escaff—Center for Climate and Resilience Research, Universidad de Chile, Santiago, Chile; Muñoz—Geophysics Department, Universidad de Chile, Santiago, Chile; Jubier—IAU, Paris, France; Lazzara—Antarctic Meteorological Research and Data Center, University of Wisconsin–Madison, and Madison Area Technical College, Madison, Wisconsin; Keller—Antarctic Meteorological Research and Data Center, University of Wisconsin–Madison, Madison, Wisconsin; Rojo—Astronomy Department, Universidad de Chile, Santiago, Chile

olar eclipses are impressive astronomical events that have attracted people's curiosity since ancient times. On average, a total solar eclipse (TSE) occurs approximately every 18 months on Earth, but a given location experiences a TSE only once every ~380 years (Meeus 1982). Through occultation of the sun by an aligned passage of the lunar disk, TSEs temporarily restrict incident radiant energy from reaching Earth's atmosphere. Subsequent responses to eclipses span environmental systems from subsurface soil layers to the ionosphere (Anderson 1999; Colligan et al. 2020; Eaton et al. 1997; Fernández et al. 1993; Founda et al. 2007; Hanna 2000; Zerefos et al. 2007; Zhang et al. 2017; Mahmood et al. 2020) and include transient variations in air temperature, relative humidity, wind speed, atmospheric gravity waves, and turbulence within the boundary layer. The temporal and spatial predictability of eclipses, along with their abrupt alterations to the radiation balance, have made them especially interesting events for atmospheric research. Most studies on "eclipse meteorology" rely on ad hoc and regular measuring platforms over continental landmasses to characterize local or regional impacts. A review of these studies is presented, among others, by Harrison and Hanna (2016) and Aplin et al. (2016). Besides changes in incoming solar radiation, the impact more readily evident of solar eclipses is the reduction in surface and near-surface (e.g., 2 m AGL) air temperature occurring within minutes of the eclipse maximum and varying between 0° and 10°C [see, for instance, Table 1 in Kameda et al. (2009)]. In some cases, the perturbation of the surface wind is marked (up to 2 m s⁻¹) but the so-called eclipse winds have been more elusive to detect and diagnose (Aplin et al. 2016; Gray and Harrison 2016). Overall, relatively few studies have been conducted with a focus on the Southern Hemisphere (SH) and only one TSE (23 November 2003) has been described over Antarctica (Pasachoff 2012; Kameda et al. 2009).

On 4 December 2021—a few days before SH summer solstice—the moon blocked the sun over high latitudes of the SH producing varying degrees of obscuration (ω : the fraction of the sun's area occulted by the moon) over Antarctic and surrounding seas (Figs. 1a,b). An overview of Antarctic geography and climate is included in the sidebar. The event lasted ~2 h from the first (C1) to the fourth contact (C4) between the lunar and solar disks. Total obscuration (totality) lasted up to 1 min in places within a band ~420 km wide arching from the southwest Atlantic to the Amundsen Sea and passing over the Ronne–Filchner Ice Shelf and Ellsworth Land. Because of Earth's rotation and lunar displacement, the maximum obscuration was not simultaneous, occurring around 0700 UTC in the Atlantic sector and one hour later in the Amundsen Sea (Fig. 1c). Likewise, the sun's elevation above the horizon near the time of totality varied from near 0° to 40° (Fig. 1d).

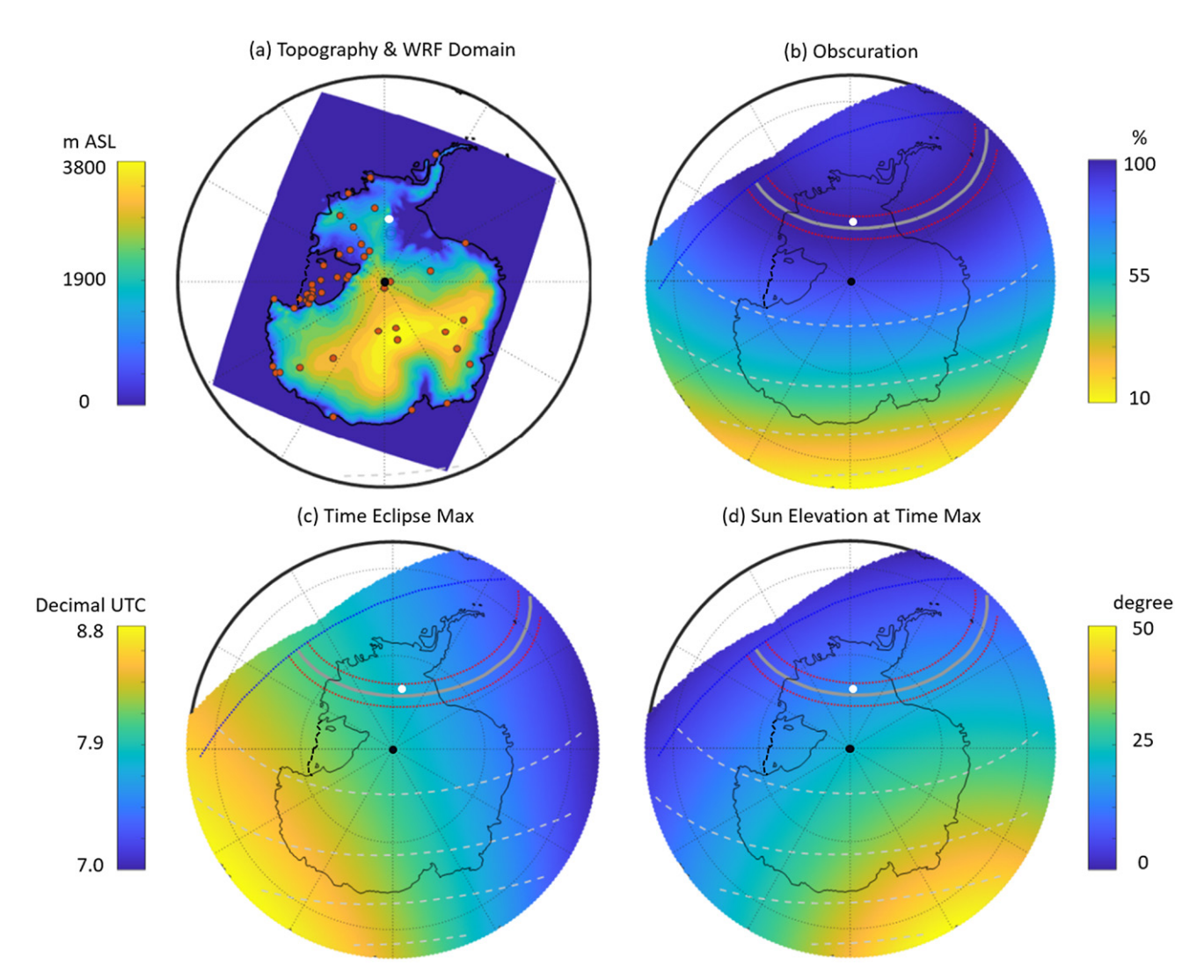


Fig. 1. Local circumstances of the 4 Dec 2021 total solar eclipse over Antarctica. (a) Terrain elevation and location of meteorological stations (see supplemental Table 1 for further information). The white and black circles are Union Glacier camp and South Pole Observatory, respectively. (b) Obscuration (ω : fraction of the sun's area occulted by the moon) caused by this eclipse. The red lines enclose the region where the eclipse was total (ω = 100%). The white dashed lines are isolines ω = 80%, 60%, 40% and 20%. (c) Time—in decimal UTC—when the sun's obscuration was maximum during 4 Dec 2021. (d) Elevation of the sun over the horizontal at the time of the eclipse maximum.

In this work, we describe the effect of the 4 December 2021 TSE on surface meteorology, especially the eclipse-induced changes in air temperature, pressure, and winds. Adding to the growing body of literature on eclipse meteorology, our effort takes advantages of the seemingly homogeneous land surface of Antarctica and the well-known astronomical circumstances of the TSE to disentangle the various atmospheric processes contributing to the meteorological impacts of eclipses. Instead of the traditional scientific paper structure (data and methodology, results, discussion), we organize this work aiming to understand the heterogenous spatial distribution of TSE cooling using self-contained but interrelated approaches. The methodological specificities of these approaches are presented in appendixes A–C. We start by documenting the observed temperature change during the TSE across Antarctica using meteorological field campaign observations at Union Glacier and in situ meteorological observations from 40 stations with varying eclipse magnitudes from 100% to 40% (second section). In the third section we use a very simple surface energy balance model to interpret the disparate temperature changes. Even when including the cloud effect—a challenge in itself—the simple model only accounts for the broad features of the TSE-induced cooling, calling for the use of a full-physics model to diagnose this impact. This is addressed in the fourth

Antarctica—Geographic and climatic context

The Antarctic continent covers about 14 million km² located to the south of the Antarctic Circle (66.4° S)—except for the northern tip of the Antarctic Peninsula—thus experiencing \sim 6 months of permanent darkness and \sim 6 months of permanent light. Since its glaciation at the Eocene—Oligocene transition \sim 34 million years ago (Kennedy et al. 2015), the Antarctic bedrock has been covered by an ice layer that currently averages up to \sim 2 km thick, holding around 90% of the world's freshwater as ice (King and Turner 1997) and hosting the coldest places on Earth (Scambos et al. 2018). The continent is often divided into West and East Antarctica, two geologically distinct areas separated by the Transantarctic Mountains (Fig. 1a). The topography of West Antarctica is relatively low, except along the Antarctic Peninsula, with an average elevation of around 1,500 m MSL. The Ross Ice Shelf, the largest ice shelf of Antarctica, is a part of West Antarctica. East Antarctica is dominated by the high Antarctic Plateau (or dome), rising quickly inland from the coast, averaging 2,500 m MSL or greater (King and Turner 1997).

Moisture-laden air masses are transported from lower latitudes toward the Antarctic periphery by atmospheric rivers (Gorodetskaya et al. 2014; Bozkurt et al. 2018; Wille et al. 2021), though these events seldom reach the interior of the continent. Extremely dry air aloft enhances the radiative cooling of the snow-covered surface, resulting in an intense inversion layer at low levels (Handorf et al. 1999; Cassano et al. 2021). The stable, mostly clear, and exceptionally dry conditions over the interior of Antarctica have fueled the interest for performing astronomical observations despite obvious logistic challenges (Burton 2010; Falvey and Rojo 2016). The approximately parabolic shape of the Antarctic topography, with the highest elevations not far from its center, foster the development of strong katabatic winds draining cold air from the interior (Bromwich et al. 1992; Heinemann et al. 2019) and eventually converging with the circumpolar ring of the SH westerly winds around the Antarctic periphery (e.g., Marshall et al. 2006).

section with high-resolution numerical experiments (eclipse enabled and eclipse disabled) using the Weather Research and Forecasting (WRF-ARW v.4.3.2) Model. Model results compare favorably with our observational estimates and signal areas where radiative and dynamical conditions dominate the TSE impact. Concluding remarks are stated in the fifth section.

Observations across the Antarctic

Detailed observations at Union Glacier and South Pole. We begin our observational description of the eclipse's meteorological impact using detailed measurements at Union Glacier (UG; online supplemental Fig. 1; https://doi.org/10.1175/BAMS-D-22-0272.2) and the Amundsen–Scott South Pole Station (SPO). Every summer, the Chilean Antarctic Institute (INACH) conducts a scientific expedition at the foothills of the Ellsworth Mountains, setting up a camp over UG (79°46′10″S, 82°54′26″W; 700 m MSL). An automatic weather station is permanently maintained at this site, providing hourly measurement since 2017. Because UG was in the path of totality and has a low cloud frequency during the SH summer, a group of us (PR, RG) organized a project within the INACH expedition to acquire high-resolution meteorological data (see details in Table 1) and astronomical observations during the 4 December 2021 TSE.

The surface meteorology 10-s measurements span from 27 November to 5 December 2021, but here we focus on the TSE by showing the series of incident solar radiation (SW\$\psi\$), net radiation (NR), air (2 m AGL: T_{2m}) and snow (2 cm below surface) temperatures, and wind speed (1.5 m AGL) (Fig. 2). Given UG's location south of the Antarctic Circle, the sun is always above the horizon during summer months, but the solar elevation (χ) varies between 12° (summer "midnight") and 33° (local noon) in early December. The SW\$\psi\$ began to reduce due to the TSE at 0653 UTC (C1), about 1 h after local "midnight," culminated at 0745 UTC (τ_{max}) with totality lasting 43 s, and returned to the no-eclipse, clear-skies values by 0837 UTC (C4). The TSE thus occurred during "dawn," when UG generally experiences the coldest conditions of the day. Yet, there is an evident V-shaped eclipse-induced cooling in both the near-surface air and surface snow temperatures. In both series there is a minimum within ~10 min from

Table 1. Meteorological sensors in the automatic weather station mounted in Union Glacier Camp for the eclipse observation. All sensors were wire connected to a datalogger CR10X (Campbell Scientific) and sampled every 10s.

Variable	Sensor model	Manufacturer	Accuracy	Comments	
Air temperature	HMP60	Campbell	±0.6°C	Installed at about 2 m above ground, included solar	
Relative humidity		Scientific	±7%	shield protection	
Barometric pressure	PTB110	Vaisala	±0.5 hPa	Installed within enclosure	
Downward (incident)	CMP11	Kipp and Zonen	<2%	ISO secondary standard	
solar radiation (GHI)				Double glass dome; spectral range from 285 to 2,800 nm	
Upward (reflected) solar radiation				Installed at about 2 m above ground	
Net radiation (up + down, Vis + IR)	NR-Lite	Kipp and Zonen	$<$ 10 W m $^{-2}$ (Blonquist et al. 2009)	Spectral range: 0.2–100 μ m; installed at about 1 m above ground	
Snow temperature	109 Temp probe	Campbell Scientific	±0.6°C	Installed in the snow about 3 cm below the surface	
Wind speed and direction	Wind monitor	R. M. Young	$\pm 0.3\text{m s}^{-1}$ and $\pm 1^\circ$	Installed at about 2 m above ground	

 $\tau_{\rm max}$ and, judging qualitatively, the largest cooling relative to noneclipse conditions was ~3°C (Fig. 2b). A more objective estimate of the cooling is provided in the next section, but we note this change is similar to that at Dome Fuji (77°19′S, 39°42′E; 3,810 m MSL) during the TSE of 23 November 2003 (Kameda et al. 2009). The 10-s wind speed observations at UG were highly variable (Fig. 2c) but they show an overall strengthening during the 6 h before $\tau_{\rm max}$ followed by a marked deceleration in the next hour. Nevertheless, similarly rapid transitions occurred at other periods of the day. Furthermore, on 4 December 2021, the surface pressure exhibited a gradual decrease that went undisrupted during the TSE (not shown), so we have refrained from labeling the speed changes at UG as "eclipse wind."

SPO is located on the high plateau of Antarctica at 2,835 m MSL and operated permanently by the U.S. Office of Polar Programs of the National Science Foundation (Lazzara et al. 2012). The eclipse at SPO was partial, beginning at 0700 UTC, reaching maximum obscuration (ω = 0.91) at 0754 UTC, and ending at 0849:00 UTC 4 December 2021. At τ_{max} the sun was 22.4° above the horizon. One-minute averages of air temperature at 2, 10, and 37 m AGL (Fig. 3) reveal that before C1 there was a very weak warming and a nearly isothermal layer (at -33°C) between 2 and 10 m—suggesting the existence of surface mixed layer—capped by an inversion where temperature increased ~2°C between 10 and 37 m. This overall structure reappeared after the TSE, when the sun was higher above the horizon, but the inversion strength reduced by about half. Compared with UG, the steady conditions at SPO exhibit a more evident signature of the eclipse, especially in $T_{\rm 2m}$, where the cooling began very close to C1 and continues until 10 min after $\tau_{\rm max}$, causing a \sim 5°C decrease. Note the substantially larger cooling at SPO (partially eclipsed) compared to UG (under totality); T_{2m} remained low until C4 when it began to rise during the SPO "morning." The upper levels also experienced a cooling that began around C1, but with a smaller magnitude than at 2 m—about 2.5°C at 10 m and 1.5 °C at 37 m. Notably, the cooling at 37 m ended abruptly around $\tau_{\rm max}$ followed by a rapid warming perhaps produced by downward mixing of warmer air aloft. Similar to UG observations, the pressure and wind records at SPO did not show any obvious change during the eclipse (not shown).

Pan-Antarctic view of the eclipse-induced cooling. We now place the UG and SPO eclipse-induced cooling in a broader context of observations. The harsh conditions and largely unpopulated territory of Antarctica results in a relatively low number of ground-based meteorological observations over the continent. Contacting National Weather Services and research centers allowed us to assemble a dataset with T_{2m} records every 10 min or less from

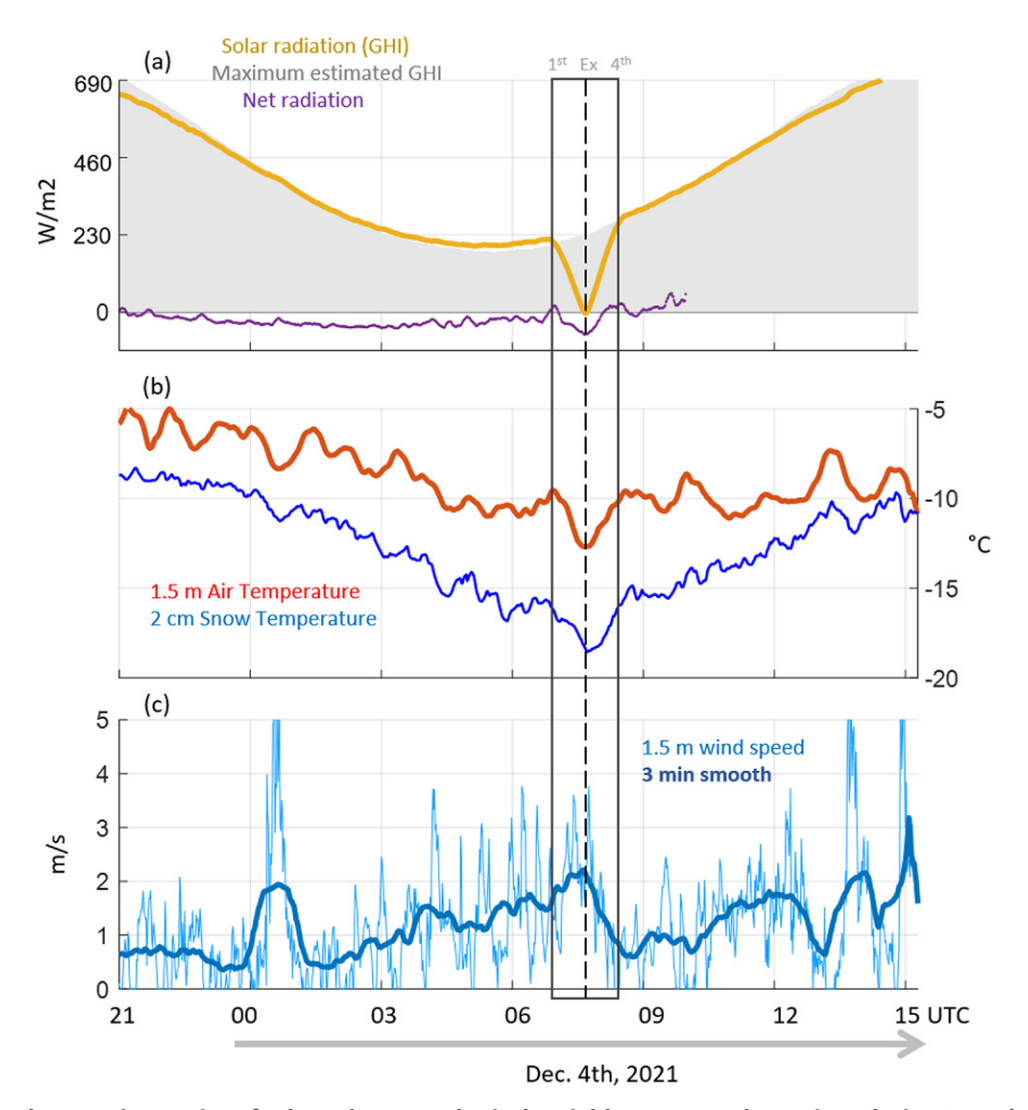


Fig. 2. The 10-s time series of selected meteorological variables measured at Union Glacier Camp (79.8°S, 82.9°W; 700 m MSL) during 4 Dec 2021. Instrument details in Table 1. The period of the eclipse—from first to fourth contact—is indicated by the rectangle and the time of the maximum by the dashed line. (a) Observed incident solar radiation (GHI; yellow line), clear sky, no eclipse estimation of incident solar radiation (gray area) and net radiation (purple line; data were lost after 1000 UTC). (b) Air temperature at 1.5 m above ground level (red line) and snow temperature at 2 cm below surface (blue line). (c) Wind speed at 1.5 m above ground level. Thin line: 10-s values; thick line: 3-min average.

37 stations across Antarctica, whose locations are shown in Fig. 1a and details are presented in supplemental Table 1. Automatic weather stations (AWS) on the Ross Ice Shelf and in West Antarctica are operated by the University of Wisconsin (UW) under the U.S. Antarctic Program (USAP). Several UW–USAP stations are also located inland from the Adelie Coast and on the Polar Plateau. Quality controlled 10-min data are available for most of these stations from the Antarctic Meteorological Research and Data Center (AMRDC) Data Repository at https://doi.org/10.48567/1hn2-nw60.

A cursory examination of the 10-min evolution of $T_{\rm 2m}$ reveals the complexity of gauging the eclipse-induced cooling from observations alone, as the signal is superimposed on the diurnal cycle and coexists with other high-frequency variations. We thus applied an objective method to all the stations in our dataset to obtain an observational estimate of the *maximum change* in $T_{\rm 2m}$ due to the solar obscuration $(\widetilde{\Delta T}_{\rm 2m}^{\rm obs})$ hereafter) and its uncertainty $(\sigma_{\rm \Delta T})$ as described in appendix A. The maximum cooling generally occurs within 30 min from $\tau_{\rm max}$. The estimates of the eclipse-induced cooling are presented in Fig. 4. On average, $\widetilde{\Delta T}_{\rm 2m}^{\rm obs} = 1.7^{\circ} \pm 0.3^{\circ}$ C but varies between 0.1° and 5.9°C among the stations. These observational estimates over Antarctica

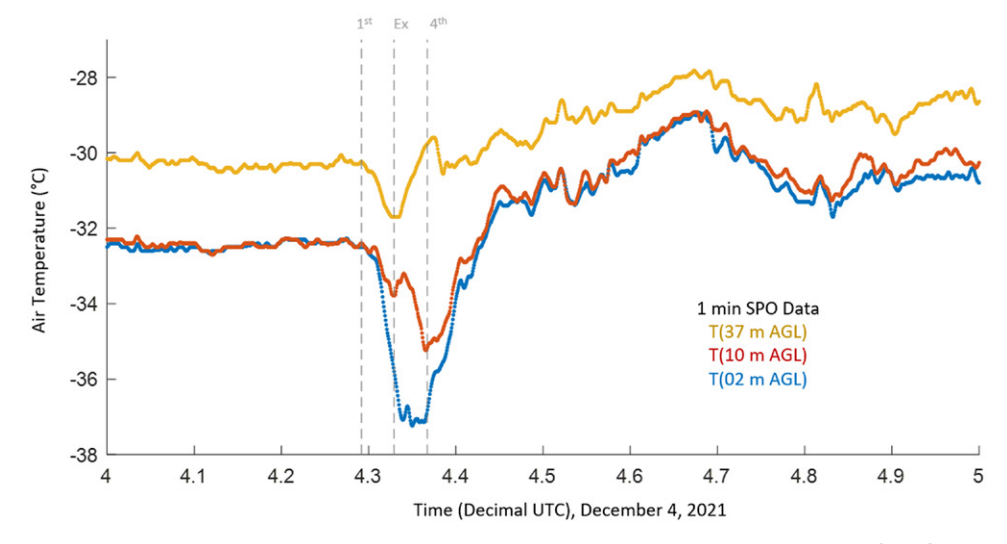


Fig. 3. The 1-min air temperature measured at Amundsen–Scott South Pole Station (SPO) at 2, 10, and 37 m above ground (blue, red, yellow lines, respectively). The time of the first and fourth contact and the eclipse maximum are indicated by vertical dashed lines.

are within the range of eclipse-induced cooling reported over other midlatitude and tropical landmasses (Aplin et al. 2016, and references therein), despite the obvious differences in surface conditions. Beyond its ample range, the most salient feature of $\widetilde{\Delta T}_{2m}^{\text{obs}}$ is that the largest values (>4°C) were not observed at the stations within the path of totality but near or over the East Antarctic dome, where obscurity (ω) was lower. For instance, $\widetilde{\Delta T}_{2m}^{\text{obs}} = 3.1^{\circ} \pm 1.5^{\circ}\text{C}$ at UG ($\omega = 1$) but reached 4.8° \pm 0.5°C at JASE 2007 ($\omega = 0.8$). In contrast, several stations with obscuration close to 100% experienced an eclipse-induced cooling <1°C, including Byrd ($\omega = 1$) in West Antarctica where $\widetilde{\Delta T}_{2m}^{\text{obs}} = 0.7^{\circ} \pm 0.9^{\circ}\text{C}$. The nonsystematic dependence of the cooling caused by the eclipse and its magnitude has been noted in previous studies (e.g., Harrison and Hanna 2016; Aplin et al. 2016) and arises from the interplay of

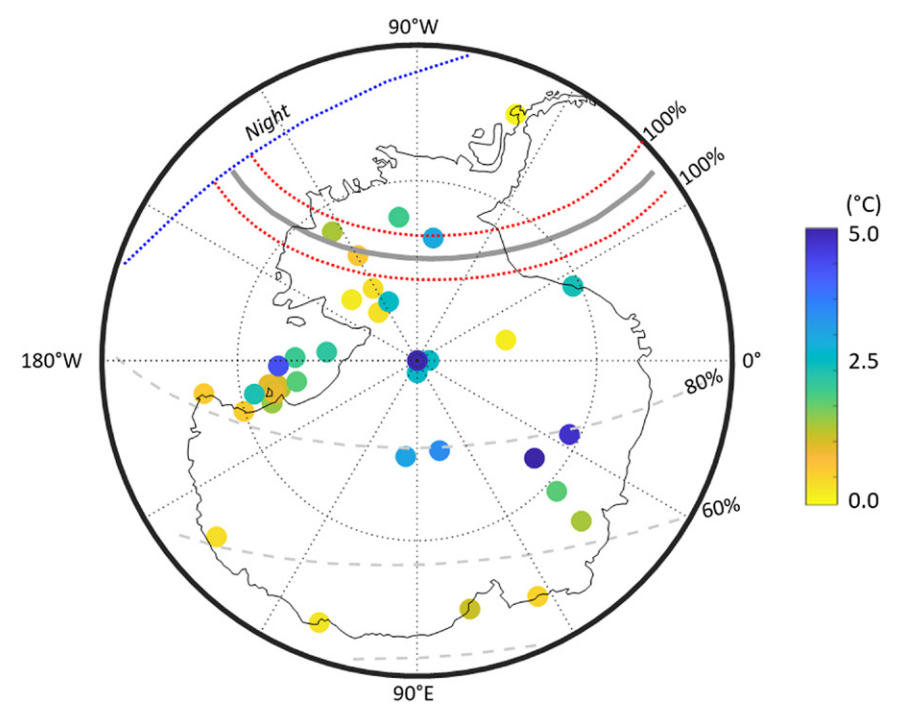


Fig. 4. Estimates of maximum cooling due to the 4 Dec 2021 total solar eclipse on selected stations across Antarctica. See appendix A for details on the cooling estimate. The red lines enclose the region where the eclipse was total ($\omega = 100\%$); the gray dashed lines are isolines $\omega = 80\%$, 60%, 40%, and 20%.

several factors, including cloud cover, baseline solar radiation, and proximity to the ocean. In the next sections these radiative and dynamical effects are explored using simple and full-physics models.

A very simple model

Most solar eclipses occur when a mixed boundary layer has already formed and they cause cooling similar to what happens in the evening transition (e.g., Segal et al. 1996). On the contrary, the TSE of 4 December 2021 occurred around "the middle of the night" across much of Antarctica, with minimum solar radiation, sensible heat toward the surface, and a surface inversion (such as in UG) or a very shallow neutral layer capped by an inversion (as in SPO). In an attempt to estimate the eclipse-induced cooling ($\Delta T_{2m}^{\rm sm}$) we developed a very simple model in appendix B (see also Fig. 5a), assuming proportionality with the eclipse-induced deficit (relative to noneclipse conditions) of the sensible heat (Δ SH) from C1 to the $\tau_{\rm max}$, so that $\Delta T_{2m}^{\rm sm} = 2\Delta$ SH $/(\rho c_p H^*)$. Here ρ is the air density, c_p is the specific heat, and H^* is the depth of the surface layer affected by the cooling. The measurements at UG were used to obtain observational estimates of two critical parameters to calculate $\Delta T_{2m}^{\rm sm}$: the eclipse-induced deficit of sensible heat (Δ SH) and H^* . Gauging the terms of the surface energy balance we found that Δ SH is very close to the eclipse-induced net solar radiation deficit (Δ SW) integrated between C1 and $\tau_{\rm max}$, and that $H^*=35$ m results in model cooling (3.1°C) closest to the observed value.

Although this is a very simple model, it is tempting to apply it over the rest of Antarctica to obtain a spatial distribution of $\Delta T_{\rm 2m}^{\rm sm}$ assuming $\Delta {\rm SH} \approx -\Delta {\rm SW}$ as well as $H^*=35$ m everywhere. No radiative measurements are available in other stations but in appendix B (see also Fig. 5b) we show that, under clear-skies (cs) conditions, the solar radiation deficit can be obtained as $\Delta {\rm SW} \approx (1/2)\omega(1-\alpha){\rm SWF}\downarrow_{\rm ne}\Delta t$, where ${\rm SWF}\downarrow_{\rm ne}$ is the incident solar radiation flux (instantaneous value) that would have occurred at the time of maximum eclipse (function of χ , Fig. 1d), ω is the eclipse obscuration, Δt is half the duration of the eclipse (from C1 to $\tau_{\rm max}$, Fig. 1c), and $\alpha=0.8$ is the snow albedo (Cuffey and Paterson 2010). Astronomical calculations (from http://xjubier.free.fr/en/index_en.html) enable us to precisely determine the values of χ , ω , and Δt at any point and thus proceed with the calculation of $\Delta T_{\rm 2m}^{\rm sm}$. Because of the prominent topography of Antarctica, air density varied in the domain following the standard atmosphere.

Figure 5c shows the results of this calculation, with $\Delta T_{\rm 2m}^{\rm sm}$ ranging from 0.5° to 5°C. The maximum eclipse-induced cooling does not occur along the path of totality but over the East Antarctic dome where obscuration (ω) was ~85%. This is because the relatively lower obscuration was compensated by the much higher elevation of the sun at the time of the TSE ($\chi \approx 38^{\circ}$), thus maximizing the term [csSWF $\downarrow_{\rm ne}\omega$]. In other words, the magnitude of the eclipse-induced cooling is dictated by the solar radiation deficit, which depends on both the obscuration (Fig. 1b) and the incident solar radiation flux that would have occurred in the absence of the eclipse around $\tau_{\rm max}$ (which, under clear skies, is proportional to the sun elevation; see Fig. 1d). Also significant, though of secondary importance, was the lower air density over the high terrain in causing the enhanced cooling in our simple model.

Although the $\Delta T_{\rm 2m}^{\rm sm}$ across Antarctica falls within the range of the observational estimates and captures the larger cooling over the East Antarctic dome, the simple model performs poorly when considering a point-to-station comparison (Fig. 5d). Among the many premises, the assumption of clear skies is not met in many places. Determining cloud cover over Antarctica is not a simple task, relying on swath data from polar-orbiting satellites. Moreover, the white and cold surface of Antarctica offers little contrast to identify clouds in either the visible or infrared channels. Using tiles from the AIRS/AMSU (flying on the EOS Aqua satellite; Molnar and Susskind 2005) between 0200 and 1200 UTC 4 December 2021, we were able to

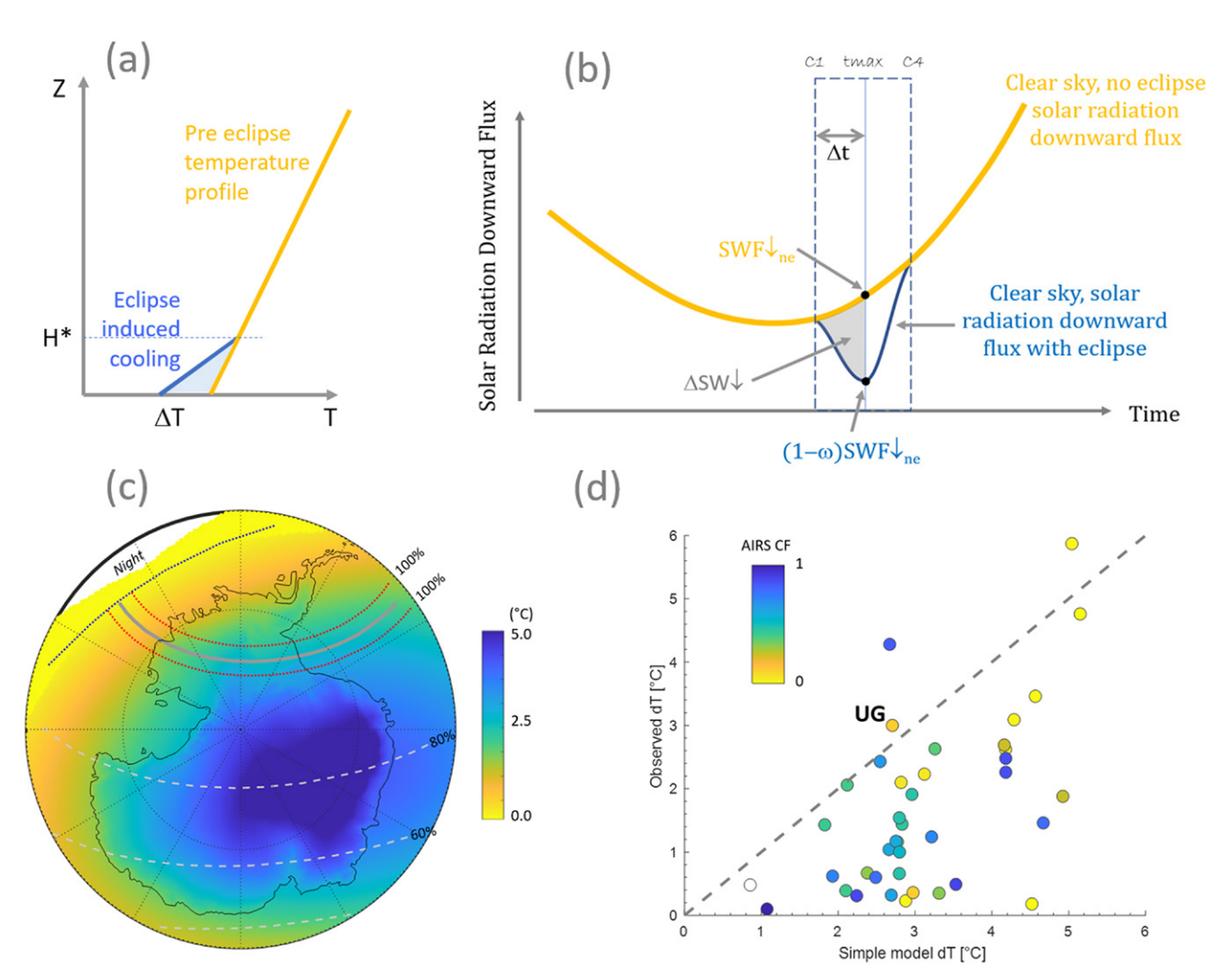


Fig. 5. Simple model estimates. (a) Schematic of the eclipse induced cooling for an event occurring when the conditions are stable. (b) Schematic effect of the eclipse on downward solar radiation flux under clear skies, with indication of the downward solar radiation deficit ($\Delta SW\downarrow$). See text and appendix B for further details. (c) Map of the maximum cooling due to the 4 Dec 2021 total solar eclipse estimated from a very simple energy balance model. The red lines enclose the region where the eclipse was total (ω = 100%), the white dashed lines are isolines ω = 80%, 60%, 40%, and 20%. (d) Scatterplot between observational and simple model estimates of the maximum cooling considering the stations data shown in Fig. 4. The symbols are color-coded according to the total cloud cover from AIRS/AMSU interpolated to each station location.

produce a cloud fraction (CF) map covering most of Antarctica (Fig. 6). This map reveals an ample band of clear skies across much of East Antarctica, including the South Pole and the high dome. Partly cloudy conditions were present along the coast facing the south Indian Ocean. The clouds over the interior of West Antarctica were patchier and we were lucky to have clear skies at UG on 4 December 2021. Mostly overcast conditions prevailed over the Ross, Amundsen, and Weddell Seas.

The interpolated AIRS CF for each station was used to color the symbols in the scatterplot between the simple model and observational estimates of $\Delta T_{\rm 2m}$ (Fig. 5d). Indeed, there is better agreement between both estimates when considering those stations under clear conditions (CF < 0.2), but the sample is reduced to nine stations and the correlation remains low. More surprisingly, there is a good agreement in stations with high CF. Because CF does not distinguish between low, middle, or high clouds, we speculate that our satellite-derived CF is not well suited to estimating the impact of cloudiness on reducing the baseline solar radiation. In addition to the challenges of better capturing the radiative component, we reiterate that our simple model does not include any dynamical effects, calling for a diagnosis of the TSE's meteorological impact based on a full-physics model, as implemented next.

A full meteorological model

We employ the WRF-ARW v.4.3.2 (hereafter WRF) Model (Skamarock and Klemp 2008; Skamarock et al. 2019) using a single model domain that covers the whole Antarctic continent at 27-km horizontal resolution on a polar stereographic projection. The WRF Model has proven to be a versatile tool for simulating complex weather phenomena in Antarctica (e.g., Bromwich et al. 2013; Deb et al. 2016; Xue et al. 2022) and is used to produce operational real-time weather forecasts for Antarctica in support of Antarctic research activities, logistics, and operational decision-making (Powers et al. 2012). On the other hand, longer runs reveal some systematic errors in clouds, radiation, and albedo (e.g., Bromwich et al.

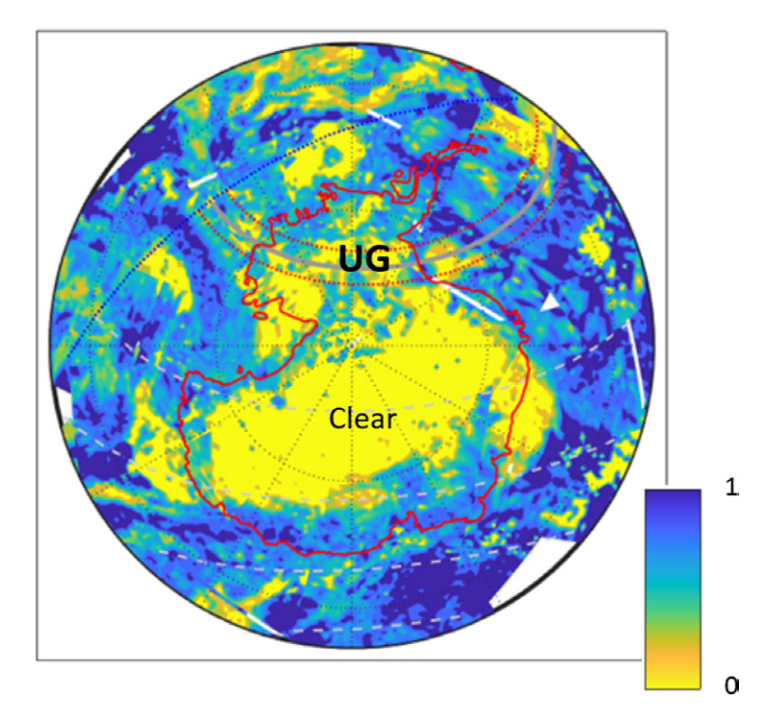


Fig. 6. Total cloud fraction over Antarctica and surrounding oceans around the time of the 4 Dec 2021 eclipse using tiles from the AIRS/AMSU between 0200 and 1200 UTC. The red lines enclose the region where the eclipse was total ($\omega=100\%$), the gray dashed lines are isolines $\omega=80\%$, 60%, 40%, and 20%.

2013; Falvey and Rojo 2016; Xue et al. 2022). Nonetheless, it is important to note that our principal focus was on analyzing very rapid changes due to the transient sun occultation. Therefore, our primary aim is not on model errors or bias, but rather understanding the impact of the eclipse. Critical to this effort is to simulate the radiation changes induced by the eclipse by activating an eclipse module (Montornès et al. 2016), which is described in more detail together with the rest of the model parameterization in appendix C and Table 2.

Our baseline experiment consists of two simulations initialized at 0000 UTC 3 December 2021 to provide the model with adequate spin-up time before the TSE. In the first simulation (WRF-nE) the eclipse module was not activated, thus providing a counterfactual simulation. A solar-eclipse simulation (WRF-E) was then performed by activating the eclipse module to simulate the actual conditions. The output files were obtained every 10 min for the whole continent and every 30 s for the grid points closest to the surface meteorological stations. Four additional experiments were performed, each consisting of a pair of WRF-E and WRF-nE integrations, initialized at different times (1200 and 1800 UTC 3 December 2021; 0000, 0600, and 1200 UTC 4 December 2021).

WRF results. The efficacy of the eclipse module implemented in WRF to simulate the changes in solar radiation due to the moon's shadow was demonstrated by Montornès et al. (2016) by comparing simulated outputs against high-resolution measurements of global horizontal irradiance for five different eclipse events and locations. To complement those findings, Fig. 7a shows downward shortwave radiation (SW↓) from WRF-nE and WRF-E at UG for 3−5 December 2021.

Before and after the TSE, the eclipse-disabled (WRF-nE) and eclipse-enabled (WRF-E) simulations are identical and in agreement with observations (Fig. 7), although the high-resolution measurements at UG exhibit substantial subhourly variability (cf. Fig. 2) and the model is about 1°C warmer before and after the TSE. The SW\ reduction in WRF-E began (ended) at

Table 2. Parameterizations used in the WRF simulations (eclipse-enabled and eclipse-disabled experiments).

Processes	Parameterization	Reference
Shortwave and longwave radiation	Rapid Radiative Transfer Model	lacono et al. (2008)
Microphysics	Thompson microphysics scheme	Thompson et al. (2008)
Boundary layer	Mellor–Yamada–Janjic (MYJ) boundary layer scheme	Janjić (1990)
Cumulus convection	Grell-Freitas ensemble cumulus scheme	Grell and Freitas (2014)
Land surface exchanges	Noah-MP land surface model	Niu et al. (2011)
Eclipse induced alteration of solar radiation	Eclipse module	Montornès et al. (2016)

C1 (C4) and went to zero at the time of eclipse maximum (τ_{max}), since UG was under totality. We further verify that the difference in SW \downarrow between WRF-nE and WRF-E was the largest at τ_{max} across the domain. The astronomical eclipse obscurity (ω) was quite close ($\pm 5\%$) to the shortwave radiation difference (in relative terms) for points with simulated CF < 0.1 and represents an upper bound for those points with higher cloudiness.

Within the modeling framework, the eclipse-induced changes in the near-surface air temperature can be readily obtained at any point as $\Delta T_{\rm 2m}^{\rm wrf} = T_{\rm 2m}^{\rm wrf-nE} - T_{\rm 2m}^{\rm wrf-E}$, where the superscript indicates the type of integration. At UG (or any other point) the series are undistinguishable until C1 because the two runs of each experiment (i.e., for a given initialization) are identical before the eclipse module is turned on. At C1 the eclipse module is activated in WRF-E and $T_{\rm 2m}^{\rm wrf-E}$ series began to cool while $T_{\rm 2m}^{\rm wrf-nE}$ began to warm (Fig. 7b). The maximum $\Delta T_{\rm 2m}^{\rm wrf}$ occurred within minutes from $\tau_{\rm max}$ and reached 4.2°C, within the range of our observational estimate (3.1° ± 1.5°C). About an hour after C4 (when the eclipse module is turned off in WRF-E) the WRF-nE and WRF-E series converge again although differences as large as 0.5°C appear until the end of the simulation. These are encouraging results, but before analyzing the remaining stations, it is worth questioning their robustness. To this end, Fig. 7c shows $\Delta T_{\rm 2m}^{\rm wrf}$ at UG for all five experiments (recall they only differ in their initialization time). As explained before, all the experiments have $\Delta T_{\rm 2m}^{\rm wrf}=0$ before C1 and then exhibit a similar cooling during the eclipse, except for the experiments initialized earlier (2 December) that simulated some clouds over UG resulting in a reduced eclipse-induced cooling. Therefore, we use the multiexperiment standard deviation of $\Delta T_{\rm 2m}^{\rm wrf}$ as a metric of modeling uncertainty. As seen in the first pair of runs, some large temperature differences appear several hours after the eclipse, but they are nonsystematic among the experiments, likely arising from divergent forecast errors as the integrations advance away from the initial conditions and after the transient activation of the eclipse module. If not detected by considering multiple experiments, such "Antarctic butterfly effect" (e.g., Sun and Zhang 2016) could have directed us to interpret some of the large posteclipse temperatures changes as a result of a mysterious phenomenon!

The modeling estimate of the eclipse-induced cooling $(\widetilde{\Delta T}_{2m}^{\text{wrf}})$ was calculated, for each grid point, as the maximum temperature difference within the eclipse period. This metric is directly comparable to the observational estimate $(\widetilde{\Delta T}_{2m}^{\text{obs}})$ as shown in the scatterplot in Fig. 8. The correlation reaches r=0.67 and, considering the observational and modeling uncertainty, most estimates are around the 1:1 line.

The spatial distribution of $\widetilde{\Delta T}_{2m}^{wrf}$ is shown in Fig. 9a. WRF simulates the largest cooling across East Antarctica, off the path of totality, with values as large as 6°C between Maud Land and the South Pole where ω ranges from 0.8 to 0.9. The cooling decays (1°–2°C) toward the Indian Ocean coast (where ω < 0.6) but also toward West Antarctica, including areas under the path of totality. Almost no cooling was found over the surrounding oceans and the Ross Ice Shelf, but one must keep in mind that SST is prescribed in our WRF simulations. Since the

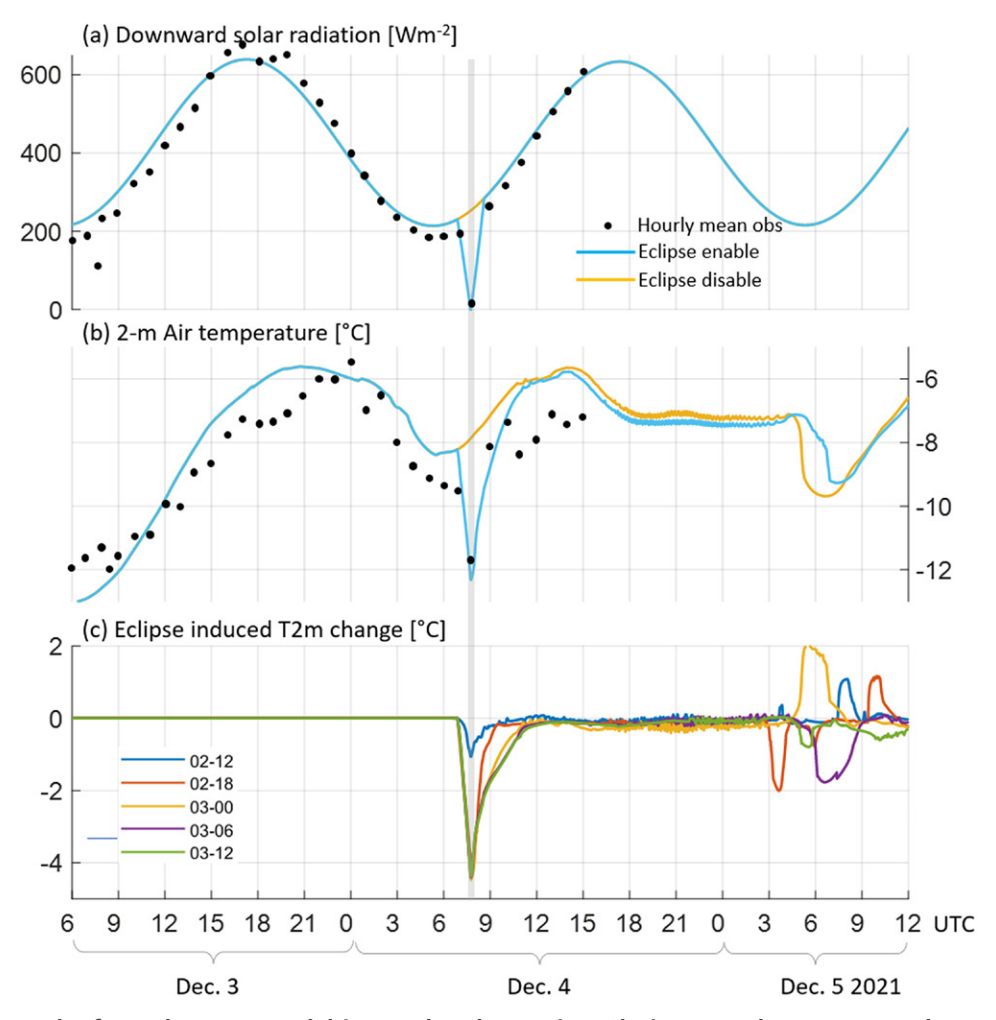


Fig. 7. Results from the WRF Model interpolated to Union Glacier camp between 3 and 5 Dec 2021. (a) Incident solar radiation and (b) 2-m air temperature. In these panels the light blue line is the result from the eclipse enable experiment and the orange line is the eclipse disable experiment. Both experiments were initialized at 0000 UTC 3 Dec 2021 and the output is 30 s. The gray vertical line indicates the time of eclipse maximum. Black dots are the hourly mean observations at UG. (c) Eclipse-induced 2-m air temperature change, calculated as the difference between the eclipse-enabled minus eclipse-disabled experiments. This difference is shown for each of the five pairs of experiments initialized between 1200 UTC 2 Dec and 1200 UTC 3 Dec 2021.

eclipse maximum obscuration occurred at different times across the continent, the cooling was also variable in time, progressing from west to east, as shown by the animations available in the online supplement.

In the vertical, the maximum cooling has a spatial pattern that mimics that at 2 m but decreases by half at 20 m and is near zero at 100 m AGL (not shown). Vertical profiles of $\Delta T_z^{\rm wrf}$ at selected stations (e.g., Nico in supplemental Fig. 2) show the attenuated propagation of the cooling signal from the surface upward with an e-folding scale of about 50 m (close to our H^\star estimate). The attenuation of the cooling with height is also evident in the SPO observations (Fig. 3). Assuming no significant pressure changes aloft during the eclipse, the integrated cooling in the lowest 100 m (Δz) above the surface induces a hydrostatic pressure change of $\Delta p_{\rm sfc}^{\rm hd} = p_{\rm sfc} (\Delta T/T_0)(\Delta z/H_0)$, where $p_{\rm sfc}$ is the reference surface pressure, T_0 is the reference temperature of the layer, ΔT is the cooling, and H_0 is the height scale calculated with T_0 . For typical values (as observed in UG), one obtains $\Delta p_{\rm sfc}^{\rm hd} \approx 0.1\,{\rm hPa}$. This value is within the range of reported pressure changes reported in eclipses elsewhere (Anderson et al. 1972). This small pressure increase was not detected in the surface observations at UG or SPO, because the sensor sensitivity is close to $\Delta p_{\rm sfc}$, but is evident in the WRF-E minus WRF-nE maximum difference

of $p_{\rm sfc}$ during the eclipse (Fig. 9b). The spatial pattern of $\Delta p_{\rm sfc}^{\rm wrf}$ also varies with time (see animations in the online supplement) lagging the $\Delta T_{\rm 2m}^{\rm wrf}$ signal by about 30 min. Whether the complex pattern of the eclipse-induced ridging drives changes in the near-surface wind field calls for further research.

Model diagnosis. The change in incident solar radiation due to the sun's obscuration without cloud effects ($\Delta SW \downarrow_{cs}^{wrf}$) varies between 0 and 270 W m⁻² across Antarctica (Fig. 10a) and acts as the primary driver of the eclipse-induced cooling as we found using the simple model. The largest values of $\widetilde{\Delta T}_{2m}^{wrf}$ increase linearly with $\Delta SW \downarrow_{cs}^{wrf}$ [~3° (100 W m⁻²)⁻¹] and occur precisely under clear skies, identified by the orange circles in the scatterplot presented in

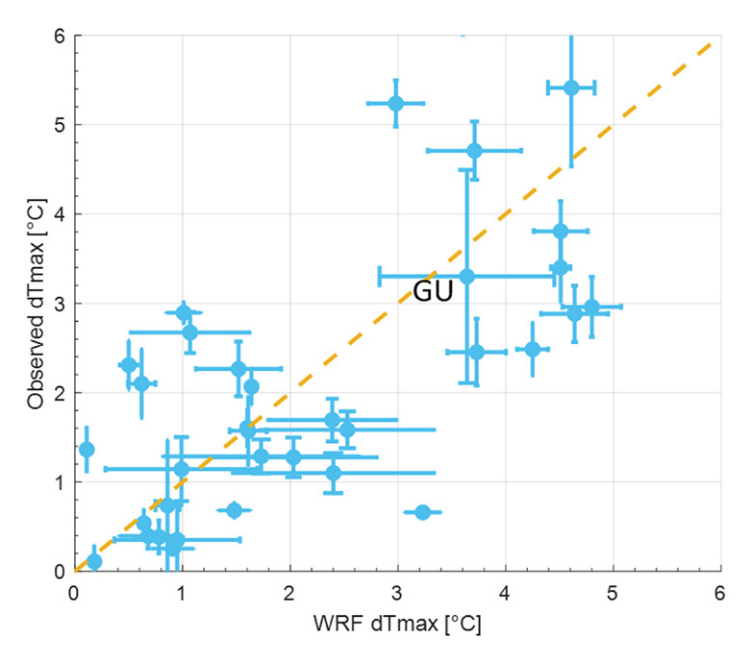


Fig. 8. Scatterplot between observational and WRF Model estimates of the maximum cooling considering the stations data shown in Fig. 4. The error bars indicate the uncertainty of these estimates. For the observations the uncertainty was calculated as the standard deviation of the estimates based on different time windows employed to define the eclipse period of influence (appendix A). For the WRF Model, the uncertainty was calculated as the standard deviation between the eclipse-induced cooling among the five pairs of experiments.

Fig. 11. However, the presence of clouds adds substantial variability to the actual change in incident solar radiation ($\Delta SW \downarrow_{cld}^{wrf}$, Fig. 10b) and can suppress the eclipse-induced cooling completely (gray circles in Fig. 11). Among other features, the effect of clouds explains the highly heterogenous cooling along the path of totality that puzzled us when examining the observations as shown in the detailed maps of the actual eclipse-induced solar radiation deficit (including the cloud effect) and $\widetilde{\Delta T}_{2m}^{wrf}$ (Fig. 12).

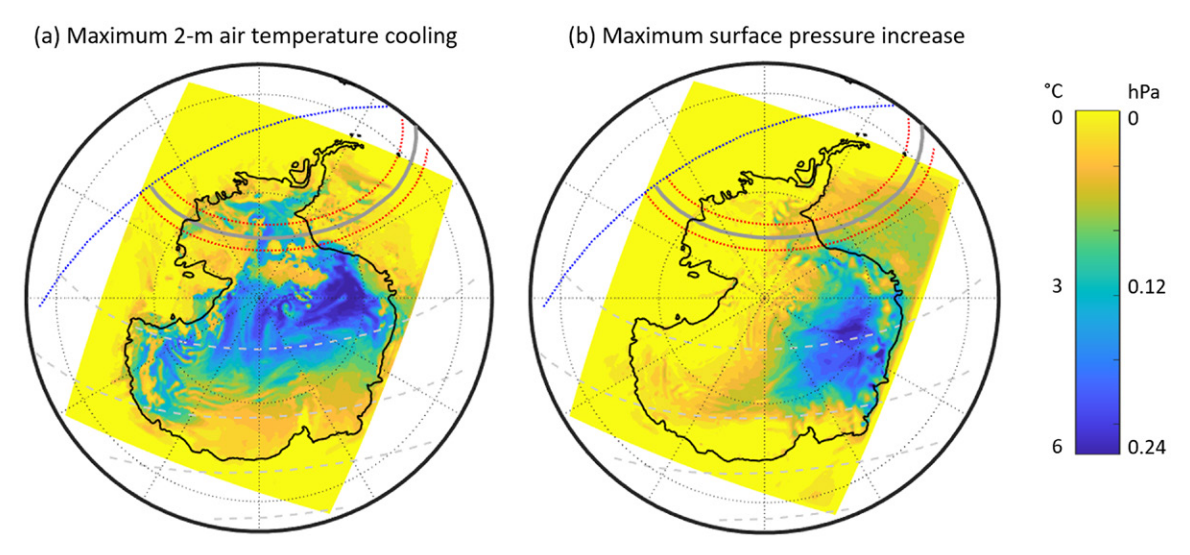


Fig. 9. (a) Spatial distribution of the WRF-simulated maximum cooling induced by the eclipse. The cooling is obtained as the difference in maximum 2-m air temperature between the eclipse-enabled minus eclipse-disabled experiments initialized at 0000 UTC 3 Dec 2021. (b) As in (a), but for the surface pressure eclipse-induced increase. The red lines enclose the region where the eclipse was total ($\omega = 100\%$); the gray dashed lines are isolines $\omega = 80\%$, 60%, 40%, and 20%.

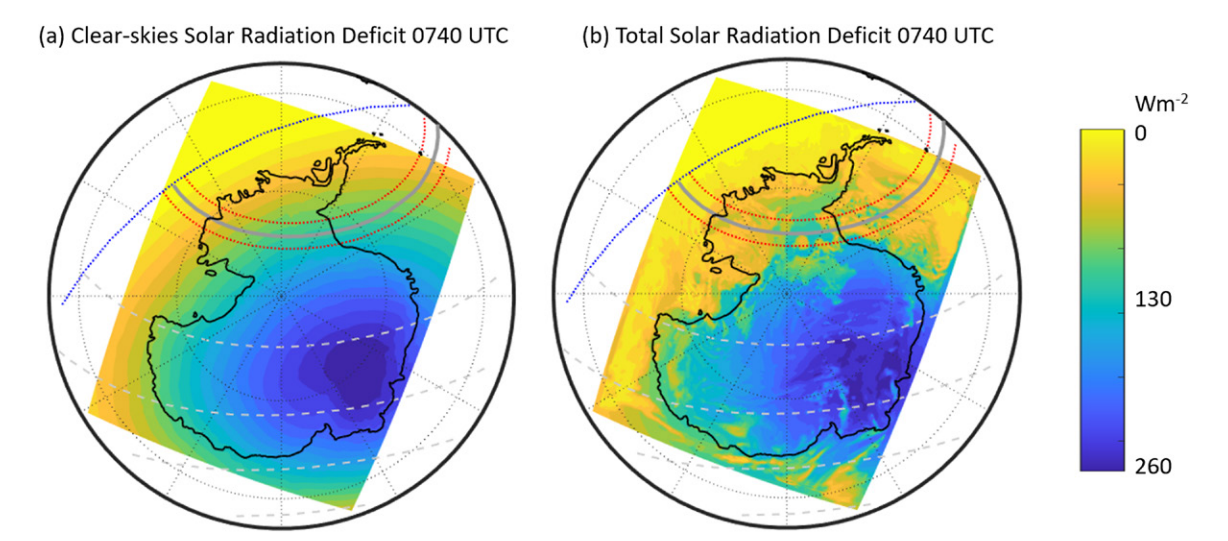


Fig. 10. (a) Spatial distribution of the WRF-simulated reduction in incident solar radiation at 0740 UTC 4 Dec 2021 (near the time of eclipse maximum) without cloud effects. The reduction is obtained as the difference in clear-skies incident solar radiation between the eclipse-enabled minus eclipse-disabled experiments initialized at 0000 UTC 3 Dec 2021. (b) As in (a), but for the actual reduction in incident solar radiation (with cloud effect). The red lines enclose the region where the eclipse was total ($\omega = 100\%$), the gray dashed lines are isolines $\omega = 80\%$, 60%, 40%, and 20%.

Beyond the cloud effect, many points in Fig. 11 with low CF and large reduction of incoming solar radiation show a significantly lower maximum cooling during the eclipse than expected (light blue circles in Fig. 11). Most of these points are located over the seaside slopes of the Antarctic dome, including parts of Dronning Maud, Kemp, Wilhelm II, and Wilkes Lands, where $\widetilde{\Delta T}_{2m}^{wrf}$ < 1°C despite the substantial reduction in incoming solar radiation induced by the eclipse (cf. Fig. 12). To understand this discrepancy, we turn to the synoptic map in Fig. 13a which shows three deep cyclones off the coast of East Antarctica on 4 December 2021, causing strong winds (>12 m s⁻¹) near the surface in these coastal areas. The strong winds advected maritime air and thus contributed to the formation of a deeper planetary boundary layer (PBL) over land (Figs. 13b,c). Indeed, this region was 3°-5°C warmer than normal the days before the eclipse (not shown). Between Dronning Maud and Enderby Lands the eclipse induced cooling was also lower than expected but the winds were not strong. The sun was higher above the horizon in that region and the deeper PBL in this region is consistent with weak sensible heat flux (\sim 30–60 W m⁻²) from the surface to the atmosphere. In contrast, the wind was quite low (<3 m s⁻¹) and the model PBL was shallow over the highest parts of the dome and most of West Antarctica.

We thus posit the existence of two regimes across the Antarctic continent that define the meteorological impact of the eclipse. The quiescent conditions over West Antarctica and most of the interior plateau set the stage for a radiative regime, in which the maximum eclipse-induced cooling was largely dictated by the actual reduction in incoming solar radiation, which in turn depends on the clear-sky "astronomical" obscuration and the presence of clouds. The strong winds over the periphery of East Antarctica led to a dynamical regime, in which the eclipse-induced cooling was very minor, irrespective of the actual $\Delta SW \downarrow_{cld}^{wrf}$, because of the strong advection of maritime air and the deep PBL in which the surface-based cooling was diluted. The inland extension of the dynamical regime is limited by the sloping terrain.

Concluding remarks

Solar eclipses represent a natural experiment upon which one can test simple and sophisticated models. The field of "eclipse meteorology" now includes the description of dozens of events but only one has been previously reported over Antarctica (23 November 2023;

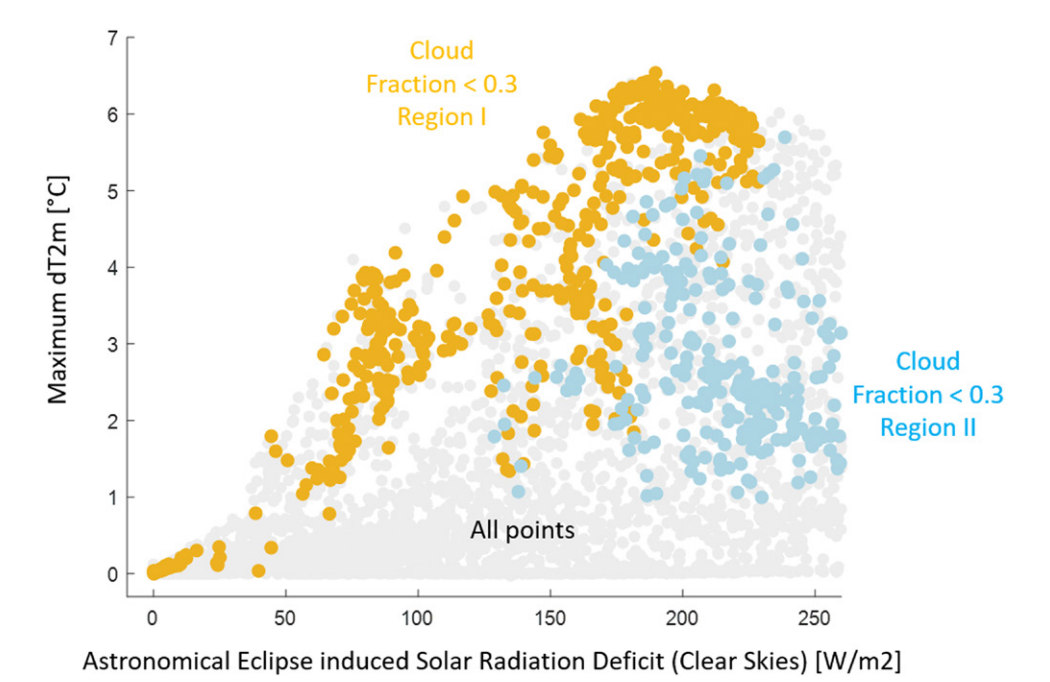


Fig. 11. Scatterplot between the eclipse-induced reduction in incident solar radiation without cloud effects and the maximum 2-m air temperature cooling across Antarctica. Each circle corresponds to a WRF grid point and is colored according to the simulated cloud cover: gray for cloud fraction over 30%, orange for cloud cover less than 30% over West Antarctica, and light blue for cloud cover less than 30%

Kameda et al. 2009). The latest event occurred on 4 December 2021, when the moon blocked the sunlight for about 2 h causing varying degrees of obscuration across the continent, including about 1 min of total obscuration within a band arching from the southeast Atlantic to the Amundsen Sea and passing over the Ronne–Filchner Ice Shelf and Ellsworth Land. Here we describe the meteorological impact of this eclipse, mainly on near surface air temperatures. A limited observational network indicates that the eclipse-induced cooling ranges between 0° and 5°C, with the most marked drop in temperatures within

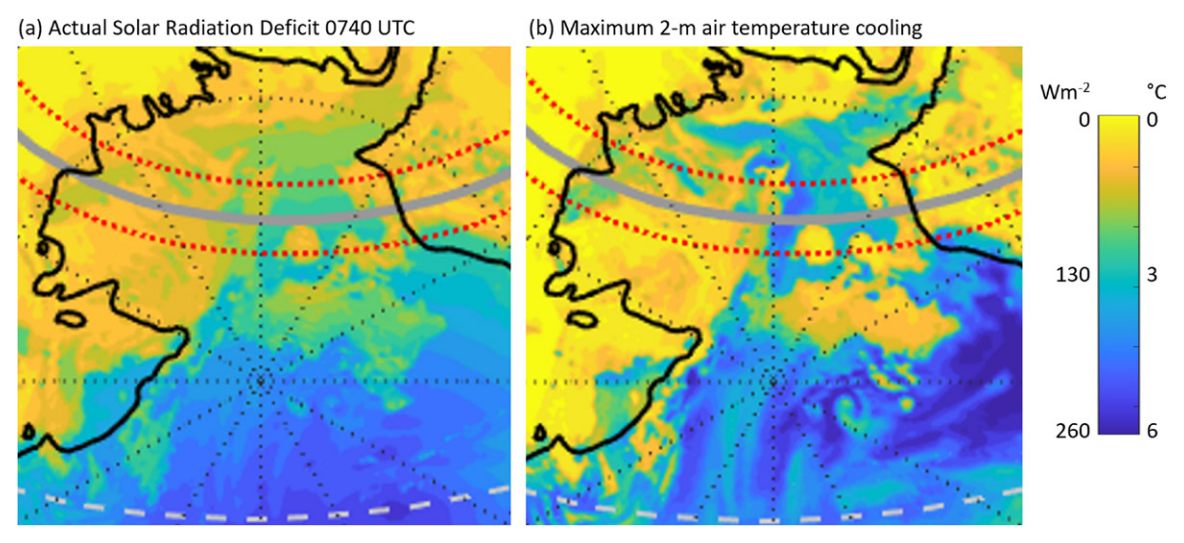
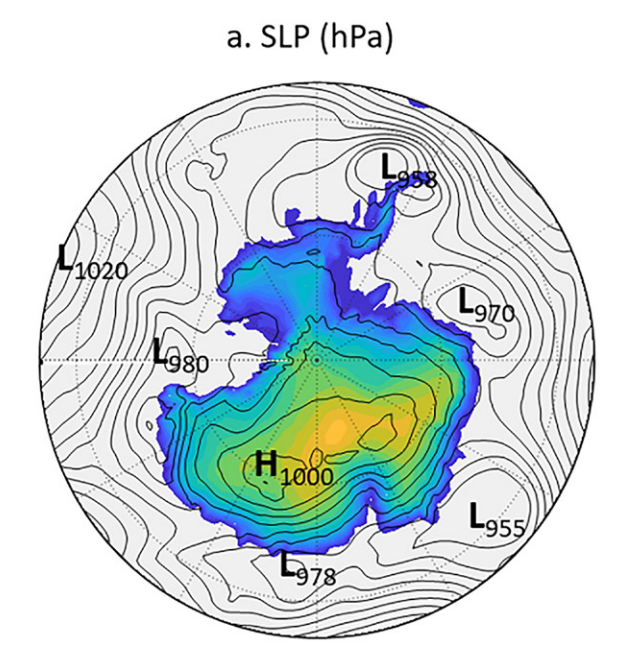


Fig. 12. (a) Spatial distribution of the WRF-simulated reduction in incident solar radiation at 0740 UTC 4 Dec 2021 (near the time of eclipse maximum) with cloud effects. The reduction is obtained as the difference in actual incident solar radiation between the eclipse-enabled minus eclipse-disabled experiments initialized at 0000 UTC 3 Dec 2021. (b) As in (a), but for the maximum 2-m air temperature cooling. Only a part of West Antarctica is shown. The red lines enclose the region where the eclipse was total (ω = 100%); the gray dashed line is isolines ω = 80%.

over east Antarctica.



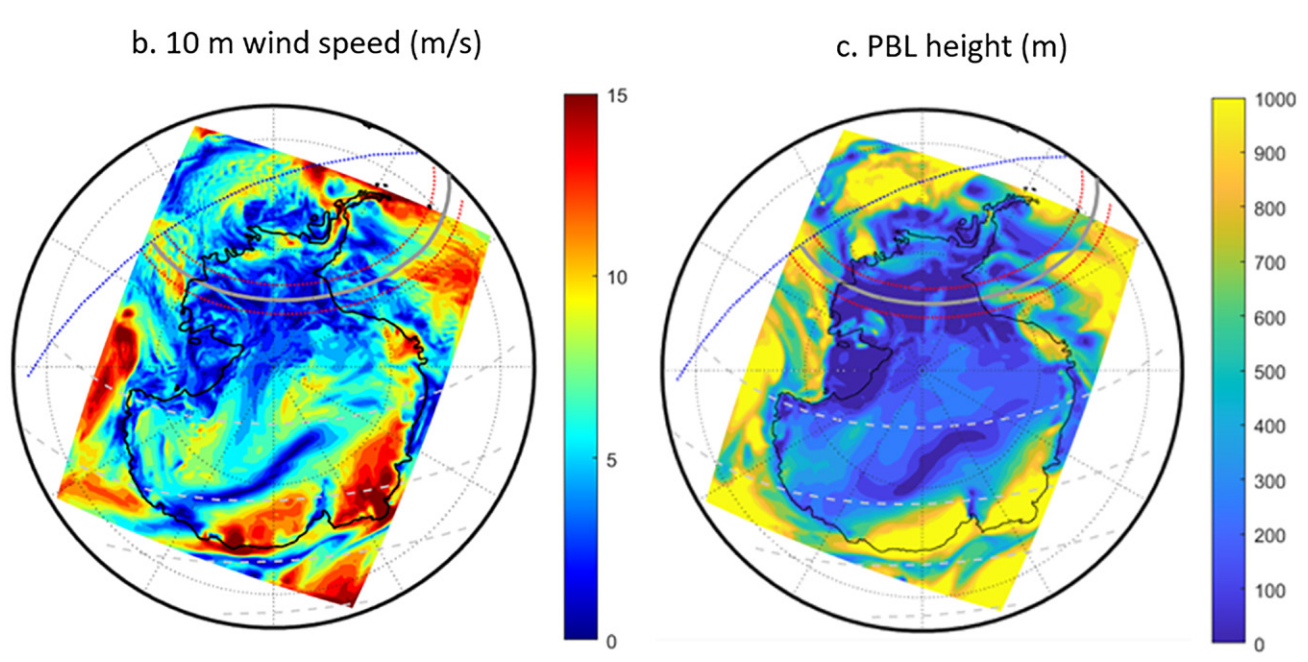


Fig. 13. (a) Sea level pressure over the Antarctic at 0800 UTC 4 Dec 2021 from ERA5. Major low pressure centers around the Antarctic periphery are identified. Color shades indicate terrain elevation. (b) WRF-simulated 10-m wind speed at 0800 UTC 4 Dec 2021. (c) As in (b), but for the planetary boundary layer height. In (b) and (c), we used outputs from the eclipse-disabled WRF simulation initialized at 0000 UTC 3 Dec 2021. The red lines enclose the region where the eclipse was total (ω = 100%); the gray dashed lines are isolines ω = 80%, 60%, 40%, and 20%.

10–20 min after the eclipse maximum. This wide range, heterogeneous cooling is at odds with the seemingly homogeneous ice-cover land surface across the continent, thus calling for further analysis.

Using a very simple surface-energy balance model, we found that, under clear skies, the maximum cooling is dictated by the solar radiation deficit which depends on the product of the obscuration and the incident solar radiation flux that would have occurred in the absence of the eclipse. This explains that, for this event, the maximum cooling took place over the plateau in East Antarctica, where obscurity was around 80% but the sun was high enough over the horizon. The presence of clouds, which were prominent near the Antarctic periphery,

breaks down this dependence and causes many sectors to experience no temperature change even if they were located under the path of totality.

The simple model is a useful tool for a rough estimate of the cooling but does not account for any dynamical effect and cloudiness has to be prescribed. To further diagnose the impact of the eclipse we used several pairs of eclipse enabled and eclipse disabled of numerical experiments using the WRF. As previously reported, the eclipse module implemented in WRF (Montornès et al. 2016) faithfully reproduces the reduction in solar radiation induced by the eclipse. The WRF-simulated cooling agrees well with the observations, especially when considering the uncertainty in both estimates, and reveals a quite complex pattern of cooling and surface pressure increase.

Within the frame of the model, the impact of cloudiness can be considered explicitly in the actual solar radiation deficit. Over most of western Antarctica there is a close relationship between the actual radiation deficit and the temperature drop, but we also found that the seaside slopes of the Antarctic dome exhibited a cooling much lower than expected. These parts of East Antarctica experienced strong winds during the eclipse, advecting warmer, maritime air inland and causing a deeper planetary boundary layer. We thus posit the existence of two regimes across the Antarctic continent that define the meteorological impact of the eclipse. The quiescent conditions over West Antarctica and most of the interior plateau set the stage for a radiative regime, in which the maximum eclipse-induced cooling was largely dictated by the actual reduction in incoming solar radiation, which in turn depends on the clear-sky "astronomical" obscuration and the presence of clouds. The strong winds over the periphery of East Antarctica led to a dynamical regime, in which the eclipse-induced cooling was very minor, irrespective of the actual solar radiation deficit, because of the strong advection of maritime air and the deep PBL in which the surface-based cooling was diluted. The inland extension of the dynamical regime is limited by the sloping terrain.

Acknowledgments. The Antarctic field work conducted by PR and RG was enabled by INACH Project RT 70-20. RG is supported by ANID/FONDAP Grant 1523A0002 (CR2). ML and LK are supported by the U.S. National Science Foundation Grant 1924730. SPO data were kindly provided by NOAA Global Monitoring Division. We are grateful to Graham Moss for his support on conducting WRF simulations. This research was partially supported by the supercomputing infrastructure of the NLHPC at Universidad de Chile. We are indebted to the INACH staff that support field operations at Union Glacier camp, especially Dr. Ricardo Jaña and Pablo Espinoza, as well as the military personnel in charge of the camp commanded by Coronel Rodrigo López Rojas from the Chilean Army.

Data availability statement. Quality-controlled 10-min data are available for most stations (supplemental Table 1) from the Antarctic Meteorological Research and Data Center (AMRDC) Data Repository at https://doi.org/10.48567/1hn2-nw60. Meteorological data from Union Glacier Camp and WRF Model outputs are available from the corresponding author (René Garreaud at Department of Geophysics, Universidad de Chile).

Appendix A: Estimating the eclipse-induced cooling from observations

Here we describe the method to obtain an observational estimate of the *maximum change* in $T_{\rm 2m}$ due to the solar obscuration along with its uncertainty $(\widetilde{\Delta T}_{\rm 2m}^{\rm obs} \pm \sigma_{\Delta T})$. For each station in our dataset, we use the original 10-min average $T_{\rm 2m}$ time series spanning the full day of 4 December 2021. A reduced time series was constructed by removing the measurements from $\tau_{\rm max}$ -60 min to $\tau_{\rm max}$ + δt , where δt varies from 60 to 120 min. This range is used to account for the variable duration of eclipse-induced cooling among the stations. Three functions were

fitted to the reduced time series (a cubic polynomial, a cubic spline, and linear), and we selected the adjusted time series as the one with the highest correlation (always the cubic spline). Finally, we obtain the residual time series as the difference between the original and adjusted series. As expected, the residuals are very small except within $[\tau_{\text{max}} - 60, \tau_{\text{max}} + \delta t]$ from which we obtain the maximum $(\Delta T_{\text{2m}}^{\text{obs}})$. In most stations there is a weak dependence of $\Delta T_{\text{2m}}^{\text{obs}}$ on the interval length (δt) and we use their standard deviation as the observational uncertainty of the eclipse-induced cooling $(\sigma_{\Delta T})$, while the difference for $\delta t = 90$ min is employed as our baseline estimate of the eclipse-induced cooling $(\widetilde{\Delta T}_{\text{2m}}^{\text{obs}})$.

Appendix B: A very simple surface energy balance to estimate the eclipse-induced cooling

The schematic of the eclipse-induced cooling presented in Fig. 5a allows to estimate its value using the expression $\Delta T_{\rm 2m}^{\rm sm} = 2\Delta {\rm SH}/(\rho c_p H^\star)$, where ρ is the air density, c_p is the air specific heat at constant pressure, H^\star is the depth of the layer affected by the cooling, and $\Delta {\rm SH}$ is the sensible heat deficit induced by the eclipse. Since this solar eclipse occurs under typically stable conditions, we assume that the cooling is not distributed uniformly with height, but it decreases linearly in the layer, which explains the factor 2 in the expression for $\Delta T_{\rm 2m}^{\rm sm}$.

Under clear skies, our simple model estimate for ΔSH is based on Fig. 5b. In a counterfactual case with no eclipse (subscript ne), the downward solar radiation flux at τ_{max} is $SWF\downarrow_{ne}$ readily obtained if the sun elevation is known. This flux is reduced to $(1-\omega)SWF\downarrow_{ne}$ with the sun obscuration. Hence, the solar radiation downward flux deficit varies from 0 at C1 to a maximum of $[1-(1-\omega)]SWF\downarrow_{ne} = \omega SWF\downarrow_{ne}$. Integrating this deficit in the time duration Δt between C1 and τ_{max} , we get $\Delta SW\downarrow \approx (1/2) \, \omega SWF\downarrow_{ne} \Delta t$. To get ΔSW , the net solar radiation deficit integrated between C1 and τ_{max} , we have to include a $(1-\alpha)$ factor, where $\alpha=0.8$ is the snow albedo. Finally, neglecting changes in longwave, evaporative, and soil-conduction energy fluxes during the eclipse we obtain $\Delta SH \approx \Delta SW \approx (1/2)\omega(1-\alpha)SWF\downarrow_{ne} \Delta t$.

Let us apply the method to the conditions at UG, where radiative measurements from the INACH station are available. By extrapolating the curve of downward solar radiative flux between C1 and C4 (Fig. 2) we estimate SWF $\downarrow_{\rm ne}$ = 250 W m⁻² at $\tau_{\rm max}$. After C1 the moon began to obscure the sun and there was a gradual decrease in the incident shortwave that culminated at $\tau_{\rm max}$ = 0744 UTC, when SW \downarrow = SW \uparrow = 0 W m⁻², so that ω = 1 and $\Delta t \sim$ 2,640 s. We note that during the period considered the snow surface cooling was <1°C, causing a minor variation of the longwave fluxes (<5%), supporting our neglect of longwave radiative effects. With the values mentioned, the sensible heat deficit results $\Delta SH \sim 66 \times 10^3$ J m⁻². The cooling estimate using this simple model depends critically on H^* . This depth scale can be estimated using a turbulence-radiative model but we have refrained from doing so given the lack of local turbulence data. Instead, we used H^* values between 20 and 60 m, which is the height range of the diurnal MBL that we observed over UG using vertical profiles acquired with a meteorological sensor (iMet-XQ2 UAV Sensor) mounted on a small drone operated several times a day at UG (supplemental Fig. 3). With these values of ΔSH and H^* , we obtain ΔT_{2m}^{sm} between 1.8° and 3.7°C, within the range of our observational estimate, and a baseline estimate $\Delta T_{2m}^{\rm sm} = 3$ °C is obtained when using $H^* = 35 \text{ m}$.

Appendix C: WRF details

The WRF-ARW v.4.3.2 Model is a state-of-the-art mesoscale numerical weather prediction model, supported and maintained by NCAR (Skamarock and Klemp 2008; Skamarock et al. 2019) and widely used to conduct limited-area numerical simulations of the atmosphere. Here we use a single model domain that covers the whole Antarctic continent, similar to the standard Antarctic CORDEX domain (Gutowski et al. 2016), at 27-km horizontal resolution on a polar stereographic projection. The domain has 181×227 grid cells and employs 60 terrain-following vertical levels between the surface and the model top at 50 hPa with

an integration time step of 30 s. Initial and boundary conditions are provided by NCEP final operational global products with a horizontal grid resolution of $0.25^{\circ} \times 0.25^{\circ}$ grids at every 6 h. Surface boundary conditions such as surface pressure, skin temperature, sea ice, and sea surface temperature are also provided from the NCEP GDAS/FNL. Land-type and topography information for the model are from the default USGS land-use data and GTOPO30 elevation data, respectively.

WRF-ARW calculates solar irradiance at the top of the atmosphere based on a solar constant of 1,370 W m⁻² modified by the day of the year (Paltridge and Platt 1976) and the cosine of the solar zenith angle, based on location of a given model grid cell, date, and time. An eclipse module (WRF-eclipse) subsequently alters the above radiation calculation through an obscuration parameter based on spatial position within the model and the positions of the sun and moon relative to Earth (Montornès et al. 2016). This module physically represents solar eclipses using an implementation of Besselian elements based on geographic position and the moon's shadow with respect to the center of Earth (Montornès et al. 2016). The present version of WRF-eclipse includes parameters offering the ability to simulate all total, partial, annular, and hybrid eclipses from 1950 to 2050 (Espenak and Anderson 2008). The WRF-ARW radiation scheme most widely tested with WRF-eclipse (Montornès et al. 2016; Spangrude et al. 2019, 2023) is the Rapid Radiative Transfer Model for GCMs (RRTMG; Iacono et al. 2008). Other parameterizations are detailed in Table 2.

References

- Anderson, J., 1999: Meteorological changes during a solar eclipse. *Weather*, **54**, 207–215, https://doi.org/10.1002/j.1477-8696.1999.tb06465.x.
- Anderson, R. C., D. R. Keefer, and O. E. Myers, 1972: Atmospheric pressure and temperature changes during the 7 March 1970 solar eclipse. *J. Atmos. Sci.*, **29**, 583–587, https://doi.org/10.1175/1520-0469(1972)029<0583:APATCD> 2.0.CO;2.
- Aplin, K. L., C. J. Scott, and S. L. Gray, 2016: Atmospheric changes from solar eclipses. *Philos. Trans. Roy. Soc.*, A374, 20150217, https://doi.org/10.1098/ rsta.2015.0217.
- Blonquist, J. M., B. D. Tanner, and B. Bugbee, 2009: Evaluation of measurement accuracy and comparison of two new and three traditional net radiometers. *Agric. For. Meteor.*, **149**, 1709–1721, https://doi.org/10.1016/j.agrformet.2009.05.015.
- Bozkurt, D., R. Rondanelli, J. Marín, and R. Garreaud, 2018: Foehn event triggered by an atmospheric river underlies record-setting temperature along continental Antarctica. *J. Geophys. Res. Atmos.*, **123**, 3871–3892, https://doi.org/10.1002/2017JD027796.
- Bromwich, D. H., J. F. Carrasco, and C. Stearns, 1992: Satellite observations of katabatic-wind propagation for great distances across the Ross Ice Shelf. *Mon. Wea. Rev.*, **120**, 1940–1949, https://doi.org/10.1175/1520-0493(1992)120 <1940:SOOKWP>2.0.CO;2.
- —, F. O. Otieno, K. M. Hines, K. W. Manning, and E. Shilo, 2013: Comprehensive evaluation of Polar Weather Research and Forecasting Model performance in the Antarctic. *J. Geophys. Res. Atmos.*, 118, 274–292, https://doi.org/10. 1029/2012JD018139.
- Burton, M. G., 2010: Astronomy in Antarctica. Astron. Astrophys. Rev., 18, 417–469, https://doi.org/10.1007/s00159-010-0032-2.
- Cassano, J. J., M. A. Nigro, M. W. Seefeldt, M. Katurji, K. Guinn, G. Williams, and A. DuVivier, 2021: Antarctic atmospheric boundary layer observations with the Small Unmanned Meteorological Observer (SUMO). *Earth Syst. Sci. Data*, 13, 969–982, https://doi.org/10.5194/essd-13-969-2021.
- Colligan, T., J. Fowler, J. Godfrey, and C. Spangrude, 2020: Detection of stratospheric gravity waves induced by the total solar eclipse of July 2, 2019. *Sci. Rep.*, **10**, 19428, https://doi.org/10.1038/s41598-020-75098-2.
- Cuffey, K. M., and W. S. B. Paterson, 2010: The Physics of Glaciers. Academic Press, 704 pp.
- Deb, P., A. Orr, J. S. Hosking, T. Phillips, J. Turner, D. Bannister, J. O. Pope, and S. Colwell, 2016: An assessment of the Polar Weather Research and Forecasting (WRF) Model representation of near-surface meteorological variables over West Antarctica. J. Geophys. Res. Atmos., 121, 1532–1548, https://doi. org/10.1002/2015JD024037.
- Eaton, F. D., J. R. Hines, W. H. Hatch, R. M. Cionco, J. Byers, D. Garvey, and D. R. Miller, 1997: Solar eclipse effects observed in the planetary boundary layer over a desert. *Bound.-Layer Meteor.*, 83, 331–346, https://doi.org/10.1023/A:1000219210055.
- Espenak, F., and J. Anderson, 2008: Total solar eclipse of 2009 July 22. NASA Goddard Space Flight Center Rep. NASA/TP-2008-214169, 86 pp., https://eclipse.gsfc.nasa.gov/SEpubs/20090722/TP214169a.pdf.
- Falvey, M., and P. M. Rojo, 2016: Application of a regional model to astronomical site testing in western Antarctica. *Theor. Appl. Climatol.*, **125**, 841–862, https://doi.org/10.1007/s00704-016-1794-x.
- Fernández, W., V. Castro, and H. Hidalgo, 1993: Air temperature and wind changes in Costa Rica during the total solar eclipse of July 11, 1991. *Earth Moon Planets*, **63**, 133–147, https://doi.org/10.1007/BF00575102.
- Founda, D., D. Melas, S. Lykoudis, I. Lisaridis, E. Gerasopoulos, G. Kouvarakis, M. Petrakis, and C. Zerefos, 2007: The effect of the total solar eclipse of 29 March 2006 on meteorological variables in Greece. *Atmos. Chem. Phys.*, 7, 5543–5553, https://doi.org/10.5194/acp-7-5543-2007.
- Gorodetskaya, I. V., M. Tsukernik, K. Claes, M. F. Ralph, W. D. Neff, and N. P. M. Van Lipzig, 2014: The role of atmospheric rivers in anomalous snow

- accumulation in East Antarctica. *Geophys. Res. Lett.*, **41**, 6199–6206, https://doi.org/10.1002/2014GL060881.
- Gray, S. R., and R. G. Harrison, 2016: Eclipse-induced wind changes over the British Isles on the 20 March 2015. *Philos. Trans. Roy. Soc.*, **A374**, 20150224, https://doi.org/10.1098/rsta.2015.0224.
- Grell, G., and S. Freitas, 2014: A scale and aerosol aware stochastic convective parameterization for weather and air quality modeling. *Atmos. Chem. Phys.*, **14**, 5233–5250, https://doi.org/10.5194/acp-14-5233-2014.
- Gutowski, W. J., Jr., and Coauthors, 2016: WCRP Coordinated Regional Downscaling Experiment (CORDEX): A diagnostic MIP for CMIP6. *Geosci. Model Dev.*, 9, 4087–4095, https://doi.org/10.5194/gmd-9-4087-2016.
- Handorf, D., T. Foken, and C. Kottmeier, 1999: The stable atmospheric boundary layer over an Antarctic ice sheet. *Bound.-Layer Meteor.*, **91**, 165–189, https://doi.org/10.1023/A:1001889423449.
- Hanna, E., 2000: Meteorological effects of the solar eclipse of 11 August 1999. Weather, 55, 430–446, https://doi.org/10.1002/j.1477-8696.2000.tb06481.x.
- Harrison, R. G., and E. Hanna, 2016: The solar eclipse: A natural meteorological experiment. *Philos. Trans. Roy. Soc.*, A374, 20150225, https://doi.org/10.1098/rsta.2015.0225.
- Heinemann, G., L. Glaw, and S. A. Willmes, 2019: Satellite-based climatology of wind-induced surface temperature anomalies for the Antarctic. *Remote Sens.*, 11, 1539, https://doi.org/10.3390/rs11131539.
- Iacono, M. J., J. S. Delamere, E. J. Mlawer, M. W. Shephard, S. A. Clough, and W. D. Collins, 2008: Radiative forcing by long-lived greenhouse gases: Calculations with the AER radiative transfer models. J. Geophys. Res., 113, D13103, https://doi.org/10.1029/2008JD009944.
- Janjić, Z., 1990: The step-mountain coordinate: Physical package. Mon. Wea. Rev., 118, 1429–1443, https://doi.org/10.1175/1520-0493(1990)118<1429:TSMC PP>2.0.CO:2.
- Kameda, T., K. Fujita, O. Sugita, N. Hirasawa, and S. Takahashi, 2009: Total solar eclipse over Antarctica on 23 November 2003 and its effects on the atmosphere and snow near the ice sheet surface at Dome Fuji. J. Geophys. Res., 114, D18115, https://doi.org/10.1029/2009JD011886.
- Kennedy, A. T., A. Farnsworth, D. J. Lunt, C. H. Lear, and P. J. Markwick, 2015: Atmospheric and oceanic impacts of Antarctic glaciation across the Eocene— Oligocene transition. *Philos. Trans. Roy. Soc.*, A373, 20140419, https://doi. org/10.1098/rsta.2014.0419.
- King, J., and J. Turner, 1997: Antarctic Meteorology and Climatology. Cambridge Atmospheric and Space Science Series, Cambridge University Press, 422 pp., https://doi.org/10.1017/CB09780511524967.
- Lazzara, M. A., G. A. Weidner, L. M. Keller, J. E. Thom, and J. J. Cassano, 2012: Antarctic Automatic Weather Station program: 30 years of polar observation. *Bull. Amer. Meteor. Soc.*, 93, 1519–1537, https://doi.org/10.1175/BAMS-D-11-00015.1.
- Mahmood, R., and Coauthors, 2020: The total solar eclipse of 2017: Meteorological observations from a statewide mesonet and atmospheric profiling systems. *Bull. Amer. Meteor. Soc.*, **101**, E720–E737, https://doi.org/10.1175/BAMS-D-19-0051.1.
- Marshall, G. J., A. Orr, N. P. van Lipzig, and J. C. King, 2006: The impact of a changing Southern Hemisphere Annular Mode on Antarctic Peninsula summer temperatures. J. Climate, 19, 5388–5404, https://doi.org/10.1175/JCLI3844.1.
- Meeus, J., 1982: The frequency of total and annular solar eclipses for a given place. *J. Br. Astron. Assoc.*, **92**, 124–126.
- Molnar, G. I., and J. Susskind, 2005: Validation of AIRS/AMSU cloud retrievals using MODIS cloud analyses. *Proc. SPIE*, **5806**, SPIE, 618–629, https://doi.org/10.1117/12.603706.
- Montornès, A., B. Codina, J. W. Zack, and Y. Sola, 2016: Implementation of Bessel's method for solar eclipses prediction in the WRF-ARW Model. *Atmos. Chem. Phys.*, 16, 5949–5967, https://doi.org/10.5194/acp-16-5949-2016.
- Niu, G. Y., Z. L. Yang, K. E. Mitchell, F. Chen, M. B. Ek, M. Barlage, and Y. Xia, 2011: The community Noah land surface model with multiparameterization options

- (Noah-MP): 1. Model description and evaluation with local-scale measurements. *J. Geophys. Res.*, **116**, D12109, https://doi.org/10.1029/2010JD015139.
- Paltridge, G. W., and C. M. R. Platt, 1976: *Radiative Processes in Meteorology and Climatology*. Elsevier, 318 pp.
- Pasachoff, J. M., 2012: Solar eclipses observed from Antarctica. *Proc. Int. Astron. Union*, **8**, 313–315, https://doi.org/10.1017/S1743921312017097.
- Powers, J. G., K. W. Manning, D. H. Bromwich, J. J. Cassano, and A. M. Cayette, 2012: A decade of Antarctic science support through AMPS. *Bull. Amer. Meteor. Soc.*, 93, 1699–1712, https://doi.org/10.1175/BAMS-D-11-00186.1.
- Scambos, T. A., G. G. Campbell, A. Pope, T. Haran, A. Muto, M. Lazzara, C. H. Reijmer, and M. R. van den Broeke, 2018: Ultralow surface temperatures in East Antarctica from satellite thermal infrared mapping: The coldest places on Earth. *Geophys. Res. Lett.*, 45, 6124–6133, https://doi.org/10.1029/2018 GL078133.
- Segal, M., R. W. Turner, J. Prusa, R. J. Bitzer, and S. V. Finley, 1996: Solar eclipse effect on shelter air temperature. *Bull. Amer. Meteor. Soc.*, 77, 89–100, https:// doi.org/10.1175/1520-0477(1996)077<0089:SEEOSA>2.0.CO;2.
- Skamarock, W. C., and J. B. Klemp, 2008: A time-split nonhydrostatic atmospheric model for Weather Research and Forecasting applications. *J. Comput. Phys.*, **227**, 3465–3485, https://doi.org/10.1016/j.jcp.2007.01.037.
- ——, and Coauthors, 2019: A description of the Advanced Research WRF Model version 4. NCAR Tech. Note NCAR/TN-556+STR, 145 pp., https://doi.org/10.5065/1dfh-6p97.
- Spangrude, C. E., D. Ross, J. W. Fowler, T. Colligan, and J. Godfrey, 2019: Validating WRF-eclipse with observations made during the 2019 total solar eclipse. 2019

- Fall Meeting, San Francisco, CA, Amer. Geophys. Union, A31M-2886, https://agu.confex.com/agu/fm19/meetingapp.cgi/Paper/521528.
- —, and J. W. Fowler, W. G. Moss, and J. Wang, 2023: Validation of the WRF-ARW eclipse model with measurements from the 2019 and 2020 total solar eclipses. *Atmos. Meas. Tech.*, **16**, 5167–5179, https://doi.org/10.5194/ amt-16-5167-2023.
- Sun, Y. Q., and F. Zhang, 2016: Intrinsic versus practical limits of atmospheric predictability and the significance of the butterfly effect. *J. Atmos. Sci.*, **73**, 1419–1438, https://doi.org/10.1175/JAS-D-15-0142.1.
- Thompson, G., P. R. Field, R. M. Rasmussen, and W. D. Hall, 2008: Explicit forecasts of winter precipitation using an improved bulk microphysics scheme. Part II: Implementation of a new snow parameterization. *Mon. Wea. Rev.*, **136**, 5095–5115, https://doi.org/10.1175/2008MWR2387.1.
- Wille, J. D., and Coauthors, 2021: Antarctic atmospheric river climatology and precipitation impacts. J. Geophys. Res. Atmos., 126, e2020JD033788, https:// doi.org/10.1029/2020JD033788.
- Xue, J., Z. Xiao, D. H. Bromwich, and L. Bai, 2022: Polar WRF V4.1.1 simulation and evaluation for the Antarctic and Southern Ocean. Front. Earth Sci., 16, 1005–1024, https://doi.org/10.1007/s11707-022-0971-8.
- Zerefos, C. S., and Coauthors, 2007: Evidence of gravity waves into the atmosphere during the March 2006 total solar eclipse. *Atmos. Chem. Phys.*, **7**, 4943–4951, https://doi.org/10.5194/acp-7-4943-2007.
- Zhang, S. R., P. J. Erickson, L. P. Goncharenko, A. J. Coster, W. Rideout, and J. Vierinen, 2017: lonospheric bow waves and perturbations induced by the 21 August 2017 solar eclipse. *Geophys. Res. Lett.*, 44, 12 067–12 073, https://doi.org/10.1002/2017GL076054.